Novel Formulations of Multireflections and Their Applications to High-Speed Channel Design

Muqi Ouyang , Student Member, IEEE, Xiao-Ding Cai, Member, IEEE, Bo Pu, Senior Member, IEEE,

Qian Gao , Srinath Penugonda, Chaofeng Li, Student Member, IEEE, Bidyut Sen,

Chulsoon Hwang[®], Senior Member, IEEE, and DongHyun Kim , Member, IEEE

Abstract—Reflection theory has been long established for over decades targeted at microwave and radio frequency (RF) applications. With ultra-high-bandwidth applications emerging, such as 112 Gb/s and higher speed Ethernet protocols, discontinuities in high-speed channels negatively impact signal quality, where

reflectionsbecomeoneofthemostcriticalconcernsinhigh-speeddesigns. In this article, for the first time, we analyzed the traditional reflection theory and proposed and verified a new formulation, which exhibits the reflection-related parameters explicitly, indicating where design optimization can be made for high-bandwidth applications using the backtracked propagation method. Our closed-form formulationisappliedtohigh-speedchannelexamples, where effective mitigation of negative impact from reflections on signal integrity can be identified to be used as a prelayout channel design guide. Our proposed formulation of the reflection theory provides more accurate prediction of high-speedchannel behavior to minimize the negative signal integrity impact from reflections.

Index Terms—Eye diagram, high-speed channel, multireflections, signal integrity.

I. INTRODUCTION

IGH-SPEED channels up to 112 Gb/s are widely used in industry protocols, commercialized through computer and communication equipment. Even though much higher speeds (224 Gb/s and above) are being conceived with cable (copper and optical) solutions, concurrent interconnections are still primarily implemented on PCBs [1]. At higher speeds, signal reflections in the channels become more severe than before due to unavoidable characteristic impedance discontinuities, in packages, connectors, pin fields, and transition vias [2], [3]. Because of low-loss materials being used for most high-speed

Manuscript received December 16, 2021; revised April 8, 2022; accepted May 8, 2022. Date of publication May 23, 2022; date of current version July 8, 2022. This work was supported in part by the National Science Foundation under Grant IIP-1916535 and in part by Cisco Systems, Inc. This paper is for the Special Section and is an expanded version from the 2021 Joint IEEE INTERNATIONAL SYMPOSIUM ON ELECTROMAGNETIC COMPATIBILITY, Signal and Power Integrity, EMC Europe. (Corresponding author: DongHyun Kim.)

Muqi Ouyang, Chaofeng Li, Chulsoon Hwang, and DongHyun Kim are with the Missouri S&T EMC Laboratory, Rolla, MO 65401 USA (e-mail: ouyangm@mst.edu; clf83@mst.edu; hwangc@mst.edu; dkim@mst.edu).

Xiao-Ding Cai, Qian Gao, Srinath Penugonda, and Bidyut Sen are with the Cisco Systems, Inc., San Jose, CA 95134 USA (e-mail: kecai@cisco.com; annagao@cisco.com; spr33@mst.edu; bisen@cisco.com). Bo Pu is with the

Detool Technology, Co. Ltd., Ningbo, Zhejiang, China (e-mail: bobpu@ieee.org).

Digital Object Identifier 10.1109/TSIPI.2022.3176592

channels for the purpose of decreasing insertion losses, reflections in the form of multireflection become more pronounced, leading to a primary cause for channel failures [4].

Theconventional high-speeddesignwouldresorttofull-wave modeling and simulation tools, which require high computational resource and time, producing desired channel performance in many cases. However, this traditional design approach may obscure the reflection mechanisms, leading designers not to know where a potential problem exists and how to solve it. As the complexity of PCB designs increases, component placement, and PCB layout become a sensitive and critical process, determining the signal integrity of the high-speed channels. In the past, component placement may be flexible with few considerations for the reflections. With the unprecedented higher speeds, a slight displacement of a critical component may incur an unforeseen channel quality disturbance, which leaves a little clue of disturbance source to the channel designers [5].

There are three major technical obstacles for high-speed signals regarding interchassis and within chassis transmissions: insertion loss, return loss, and crosstalk [4], [6]. The insertion loss issues have been mainly solved by using low loss and ultraloss materials upon proper equalization schemes. At the same time, crosstalk concerns can be mitigated by appropriate layout and spacing. The more challenging issue is return loss, which may be only solved by advanced equalization techniques. However, it is possible that there may be ways to lower the return losses with less power consumption and lower chip development costs. Theoretically, the reflection theory can explain the intricacies embedded in the channel return losses, which can lead to a technical insight on how reflection can be minimized without additional active solutions.

Reflection theory has been developed with radio frequency (RF) and microwave engineering for many decades [7], mainly limited to addressing bandlimited applications. Its applications to the high speed and high-bandwidth signal transmission emerged about 30 years ago when data rates increased to the Gb/s ranges for interchassis and within chassis communications. For instance, the first generation of PCI Express started operating at 2.5 Gb/s less than two decades ago. Since then, a few industry protocols, including Ethernet, SAS, SATA, and Infiniband, began increasing the bandwidth with a

2768-1866 © 2022 IEEE. Personal use is permitted, but republication/redistribution requires IEEE permission. See https://www.ieee.org/publications/rights/index.html for more information.

multiplier for every new generation. When Ethernet's data rates increased to the 100 Gb/s range, high-speed signals have become truly super wideband from dc to their fundamental frequencies with lower order harmonics spanning to their speed ranges in gigahertz [8].

With much higher data rates emerging in concurrent communication protocols, signal quality must be guaranteed in the wide frequency ranges without intolerable degradations, which imposes stringent requirements for understanding the reflection mechanisms. High-speed channels used in digital data communication are different from the ones used in the RF and microwave applications with the following features:

- 1) Multiple PCBs with sizable dimensions.
- 2) Hybrid connection with connectors and cables.
- 3) Cascaded interconnections with different system reference impedances.
- 4) Long transmission distance.
- 5) Thick PCB boards with up to dozens of layers.
- 6) Multiple channels running in close vicinity.
- 7) Discontinuities are separated from small tolarge distances along the transmission lines.
- 8) Involving discrete passive components such as DC block capacitors and transition vias.

All the above physical features must satisfy the same signal condition—ultrahigh bandwidth. Traditional reflection theory may seem inadequate to be applied to all the above attributes for the concerned high-speed channels.

In this article, we analyzed the reflection theory and reformulated the reflection mechanisms with a couple of new proposals targeted at the concerned high-speed channels specifically [9]-[12]. We proposed a new insertion loss formulation with reflected components represented explicitly, indicating how multireflection impacts the received signal quality in a closed-form fashion [13]. To reveal the multireflection happening between differentinterfacesformedbyinterconnectingcomponentsmodel ed with S parameters, two theoretical methods were created to quantitatively account for the reflected waves explicitly. As a validation of our unique formulations, we compared our results withthosegenerated fromcommercial tools, which confirms the accuracy of our theory.

The second part of this article shows application of our newly proposed formulations to high-speed channel optimization. Channel optimization on reflection-related structures has specialandimmediateeffectsifperformedcorrectly.Reflectionre lated structures in a normal high-speed channel are those with impedances different from what the system specifies or those with poor return loss modeled separately, also called discontinuity structures. High-impacting discontinuity structures may include vias and pins in series connection with the high-speed channels, directly degrading signal quality.

In this article, we propose a set of approaches that enable optimizing the distributed discontinuities in a high-speed channel. We tackle two different problems through our

approaches: optimizing the distance between discontinuities and optimizing

thereflections in the transmission lines based on our closed-form formulations. Our optimization targets are the minimized ripples seen at the receiver and the improved eye opening in eye diagrams, respectively, with our proposed approaches. Our results have been verified with commercial tools, confirming with high confidence.

The organization of this article is briefly summarized here. In Section II, the derivations on the closed-form formulations are discussed based on the multireflections in cascaded channels, and two methods to handle cascaded S-parameter networks are also proposed. In Section III, the accuracy of the derived formulations is validated using a numerical example. In SectionIV,themethodstooptimizecascadedchannelsarediscussed based on practical channel configurations: three segments of PCB striplines with two via transition structures. In Section V, discussions and conclusions of this article are given.

II. CLOSED-FORM FORMULATIONS

The derivation of the closed-form formulations for the insertion loss $S_{21}(\omega)$ and the group delay $t_g(\omega)$ of a single-ended cascaded channel have been discussed in detail in [13]. In the cascaded channel, each segment is modeled using a frequencydependent PCB stripline model. In this section, the formulation derivation is reviewed briefly, and the formulations are extended to handle more practical cases: differential channels with cascaded S-parameter networks.

A. Frequency-Dependent Parameters for PCB Striplines

The solutions for frequency-dependent RLGC parameters for both single-ended and differential PCB striplines are introduced in [14], and the formulations for RLGC parameters from PCB cross-sectional geometries are also presented below.

The free-space permittivity and permeability are represented as ε_0 and μ_0 , accordingly. The relative permittivity of the PCB dielectric is represented as $\varepsilon_r(\omega)$, which is frequency-dependent and complex. To ensure the causality of the system, the Djordjevic model for $\varepsilon_r(\omega)$ is implemented [15]

$$\varepsilon_r(\omega) = \varepsilon_\infty + a \cdot \ln\left(\frac{2\pi f_H + j \cdot \omega}{2\pi f_L + j \cdot \omega}\right)$$
 (1)

where ε_{∞} is the real relative permittivity value when $\omega \to \infty$; a is a constant factor; and f_L and f_H are the predefined lower and upper frequency limitations. By defining the real part of the relative permittivity $\varepsilon_{r,\omega_{0}}$ and the loss tangent $\tan \delta_{\omega_{0}}$ at a certain frequency ω_{0} , the complex relative permittivity $\varepsilon_{r}(\omega_{0})$ at frequency ω_{0} can be written as

$$\varepsilon_r(\omega_0) = \varepsilon'_{r,\omega_0} - j \cdot \varepsilon'_{r,\omega_0} \cdot \tan \delta_{\omega_0}$$
 (2)

Then, the unknown constant in the Djordjevic model ε_{∞} and a can be solved by

$$a = -\frac{\varepsilon_{r,\omega_{0}} \cdot \tan \delta_{\omega_{0}}}{\operatorname{Imag ln} \frac{2\pi f_{H} + j \cdot \omega}{2\pi f_{L} + j \cdot \omega}}$$

$$\varepsilon = \varepsilon_{r,\omega_{0}} + \varepsilon_{r,\omega_{0}} \cdot \tan \delta_{\omega_{0}} \cdot \frac{\operatorname{Real ln} \frac{2\pi f_{H} + j \cdot \omega}{2\pi f_{L} + j \cdot \omega}}{\operatorname{Imag ln} \frac{2\pi f_{H} + j \cdot \omega}{2\pi f_{L} + j \cdot \omega}}.$$
(3)

For a single-ended symmetrical PCB strip line, the cross- $_{\infty}^{\infty}$

sectional geometry is shown in Fig. 1. W and t are the width and thickness of the metal trace; b is the total thickness of the PCB dielectric; ρ is the resistance of the metal material; $G_p = 1.5$ is the factor related to the conductor loss contributed by the current in the ground plane for symmetrical striplines.

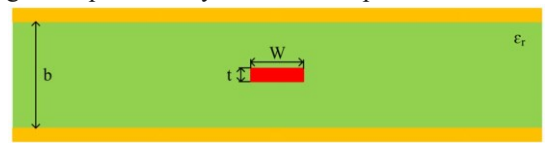


Fig. 1. Cross-sectional geometry of a single-ended symmetrical stripline.

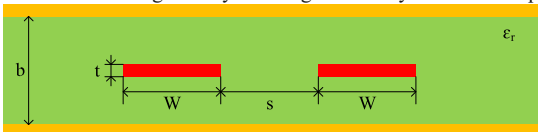


Fig. 2. Cross-sectional geometry of a differential symmetrical stripline.

When $W \gg t$, the skin-effect onset frequency is defined as

$$f_{surf} = \frac{4\rho}{t^2\pi\mu_0} \tag{4}$$

Then, the frequency-dependent RLGC parameters for the single-ended stripline are as follows:

$$\begin{cases} R_{se}(\omega) = \frac{\rho}{Wt} + \frac{\rho G_p}{Wt\sqrt{2\pi f_{surf}}} \sqrt{\omega} \\ L_{se}(\omega) = Z_{SE} \sqrt{\mu_0 \varepsilon_0 \varepsilon_r} + \frac{\rho G_p}{Wt\sqrt{2\pi f_{surf}}} \cdot \frac{1}{\sqrt{\omega}} \\ G_{se}(\omega) = \omega \frac{\varepsilon_r''}{\varepsilon_r} \cdot \frac{\sqrt{\mu_0 \varepsilon_0 \varepsilon_r}}{Z_{SE}} \\ C_{se}(\omega) = \frac{\varepsilon_r'}{\varepsilon_r} \cdot \frac{\sqrt{\mu_0 \varepsilon_0 \varepsilon_r}}{Z_{SE}} \end{cases}$$
(5)

where

$$Z_{SE} = \frac{30\pi \left(b - t\right)}{\sqrt{\varepsilon_r} \left(W + \frac{bC_f}{\pi}\right)} \tag{5a}$$

$$C_f = 2\ln\left(\frac{2b-t}{b-t}\right) - \frac{t}{b}\ln\left[\frac{t(2b-t)}{(b-t)^2}\right].$$
 (5b)

The cross-sectional geometry of a differential symmetrical PCB stripline is shown in Fig. 2. In addition to the single-ended stripline cross-section, the spacing between the two signal conductors is defined as *s*.

Toinvestigatethesignalpropagationsandreflectionsindifferenti alchannels,thefocusshouldbeontheoddmodecharacteristicsofthesystem.SimilartothesingleendedRLGCparameters, the odd-mode RLGC parameters of a

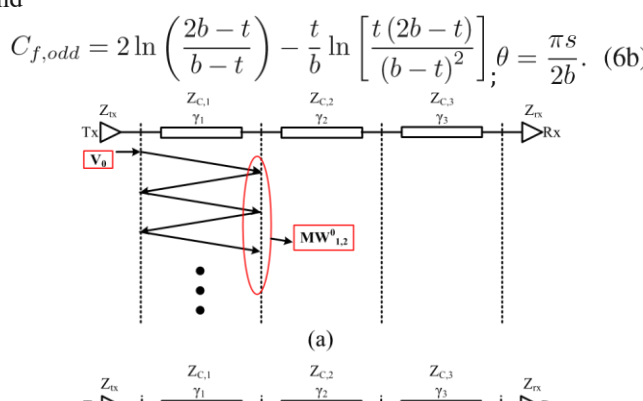
differential stripline can be written as

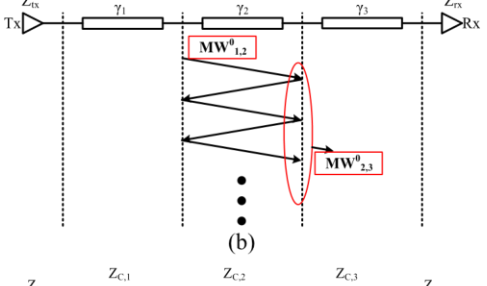
$$\begin{cases} R_{odd}(\omega) = \frac{\rho}{Wt} + \frac{\rho G_p}{Wt\sqrt{2\pi f_{surf}}} \sqrt{\omega} \\ L_{odd}(\omega) = Z_{ODD}\sqrt{\mu_0 \varepsilon_0 \varepsilon_r} + \frac{\rho G_p}{Wt\sqrt{2\pi f_{surf}}} \cdot \frac{1}{\sqrt{\omega}} \\ G_{odd}(\omega) = \omega \frac{\varepsilon_r''}{\varepsilon_r} \cdot \frac{\sqrt{\mu_0 \varepsilon_0 \varepsilon_r}}{Z_{ODD}} \\ C_{odd}(\omega) = \frac{\varepsilon_r'}{\varepsilon_r} \cdot \frac{\sqrt{\mu_0 \varepsilon_0 \varepsilon_r}}{Z_{ODD}} \end{cases}$$
(6)

where

$$Z_{ODD} = \frac{30\pi (b - t)}{\sqrt{\varepsilon_r} \left[W + \frac{bC_{f,odd}}{2\pi} \left(1 + \ln \left[1 + \frac{\tanh(\theta)}{\ln 2} \right] \right) \right]}$$
 (6a)

and





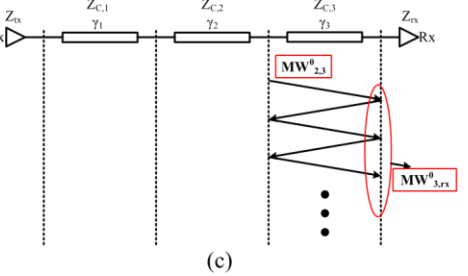


Fig. 3. Example of three cascaded striplines and wave propagations and reflections in (a) the first stripline; (b) the second stripline; and (c) the third stripline; all intrasection reflections.

For both the single-ended and the odd mode in the differential systems, the frequency-dependent characteristic impedance $Z_{\mathcal{C}}(\omega)$ and the propagation constant $\gamma(\omega)$ can be calculated using $RLGC_{se}(\omega)$ and $RLGC_{odd}(\omega)$, respectively:

$$Z_{C}(\omega) = \sqrt{\frac{R(\omega) + j\omega L(\omega)}{G(\omega) + j\omega C(\omega)}}$$
(7)

$$\gamma(\omega) = \sqrt{[R(\omega) + j\omega L(\omega)] \cdot [G(\omega) + j\omega C(\omega)]}.$$
 (8)

Then, the signal reflections and transmissions at the interfaces between different segments and the signal propagations inside each segment in the cascaded channel can

be evaluated using the derived frequency-dependent $Z_c(\omega)$ and $\gamma(\omega)$.

B. Cascaded Channel With Transmission-Line Segments

For both the single-ended and the differential systems with cascaded transmission-line segments, the method presented in [13] can be used to derive the closed-form formulations for the insertion loss $S_{21}(\omega)$ of the system.

In Fig. 3, a cascaded channel with three stripline segments and the wave propagations and reflections in each individual segment is shown.

 $Z_{C,i}$ and γ_i (i = 1,2,3) are the characteristic impedances and the propagation constants of each segment of stripline, and the lengths of striplines are l_1 , l_2 and l_3 . Z_{tx} and Z_{rx} are the impedances of the transmitter and the receiver. The wave incident from the transmitter to the first stripline segment is V_0 , and $MW_{i,j}$ 0 indicates the group of multiple waves incident from stripline segment i to stripline segment j. The transmission coefficient and the reflection coefficient from the stripline segment i to the stripline segment j are

$$T^{i,j}(\omega) = \frac{2Z_{C,j}(\omega)}{Z_{C,j}(\omega) + Z_{C,i}(\omega)}$$

$$\Gamma_{i,j}(\omega) = \frac{Z_{C,j}(\omega) - Z_{C,i}(\omega)}{Z_{C,j}(\omega) + Z_{C,i}(\omega)}$$
(9)

Notice that both the transmission coefficients and reflection coefficients defined in (9) and (10) have a directional indication. To simplify the formulation writing, for a cascaded channel with N segments, let the subscript i or j represent the transmitter or the receiver when the value is 0 or N + 1, respectively. For example, $Z_{C,0} = Z_{tx}$, $Z_{C,N+1} = Z_{rx}$, $T_{0,1} = Z_{tx}$

$$\begin{array}{ll} MW_{N,N+1} = MW_{N,rx} & \text{Ttx,1, } \text{Tn+1,N} = \text{Trx,N, } \Gamma_{1,0} = \Gamma_{1,tx}, \\ & \Gamma_{N,N+1} = \Gamma_{N,rx}, \text{ and} \\ & \dots, N & \text{In (9) and (10), } i = 0,1,\dots,N+1, \\ j = 0,1 & +1, \text{ and } i \neq j. \end{array}$$

Then, the wave incident from the first stripline to the second stripline is

$$MW_{1,2}^{0}(M)$$

$$= V_0 \operatorname{T}_{tx,1} \operatorname{T}_{1,2} e^{-\gamma_1 l_1} \left(1 + \Gamma_{1,2} \Gamma_{1,tx} e^{-2\gamma_1 l_1} + \Gamma_{1,2}^2 \Gamma_{1,tx}^2 e^{-2\gamma_1 l_1} + \cdots + \Gamma_{1,2}^M \Gamma_{1,tx}^M e^{-2M\gamma_1 l_1} \right)$$

$$= V_0 \operatorname{T}_{tx,1} \operatorname{T}_{1,2} e^{-\gamma_1 l_1} \frac{1 - \left(\Gamma_{1,2} \Gamma_{1,tx} e^{-2\gamma_1 l_1} \right)^{M+1}}{1 - \Gamma_{1,2} \Gamma_{1,tx} e^{-2\gamma_1 l_1}}$$

$$= V_0 \operatorname{T}_{tx,1} \operatorname{T}_{1,2} e^{-\gamma_1 l_1} CM_1 (M)$$
(11)

where M = 0,1,2,... is defined as the number of wave reflections in the same stripline segment, and

$$CM_{i}(M) = \frac{1 - (\Gamma_{i,i+1}\Gamma_{i,i-1}e^{-2\gamma_{i}l_{i}})^{M+1}}{1 - \Gamma_{i,i+1}\Gamma_{i,i-1}e^{-2\gamma_{i}l_{i}}}.$$
(12)

Generally, due to the loss and reflections:

$$\left|\Gamma_{i,i+1}\Gamma_{i,i-1}e^{-2\gamma_i l_i}\right| < 1$$

Therefore,

$$\lim_{M \to \infty} CM_i(M) = \frac{1}{1 - \Gamma_{i,i+1} \Gamma_{i,i-1} e^{-2\gamma_i l_i}}$$
(13)

and the incident wave including infinite number of reflections is

$$\lim_{M \to \infty} MW_{1,2}^{0}(M) = \lim_{M \to \infty} V_{0} T_{tx,1} T_{1,2} e^{-\gamma_{1} l_{1}} CM_{1}(M)$$

$$= V T_{tx,} T_{1,2} e^{-\gamma_{1} l_{1}} e^{-\gamma_{1} l_{1}} CM_{1}(M)$$

$$= V T_{tx,1} T_{1,2} e^{-\gamma_{1} l_{1}} CM_{1}(M)$$

The superscript 0 in $^{MW^0_{1,2}}$ indicates zeroth orders of reflections between different segments, which will be defined more specifically later.

Similarly, the wave incident from the second stripline to the third stripline and the wave incident to the receiver can be

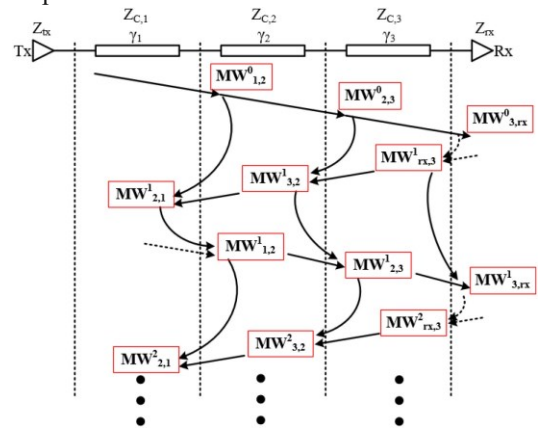


Fig. 4. Wave reflections between multiple transmission line segments; all intersection reflections.

calculated:

$$MW_{20,3}(M) = MW_{10,2}(M) \cdot T_{2,3}e_{-\gamma_2 l_2}CM_2(M)$$
 (15)

$$MW_{30,rx}(M) = MW_{20,3}(M) \cdot T_{3,rx}e_{-\gamma_{3}l_{3}}CM_{3}(M).$$
 (16)

Based on (11), (12), (15), and (16), a more generalized formulation for the incident wave in a cascaded transmission line system with *N* segmentations can be written as

$$MW_{A,A+1}^{0}(M) = V_{0} T_{tx,1} \prod_{i=1}^{A} \left[e^{-\gamma_{i} l_{i}} \cdot T_{i,i+1} \cdot CM_{i}(M) \right]$$
(17)

for $1 \le A \le N$.

Then, the reflections between multiple segments need to be evaluated, as shown in Fig. 4.

In Fig. 4, ${}^{MW}{}_{i,j}^{M'}$ indicates the total wave incident from stripline segment i to stripline segment j, and the superscript M

is defined as the number of reflections and transmissions between multiple stripline segments.

Becausethereisnofurtherdiscontinuity beforethetransmitter and after the receiver, there is no wave reflecting into the first segment or reflecting back at the last segment, which are marked with dashed arrows in Fig. 4, and for $M^\prime>0$

$$MW_{0,1}^{M'}(M) = MW_{tx,1}^{M'}(M) = 0$$

$$MW_{N+1,N}^{M'}(M) = MW_{rx,N}^{M'}(M) = 0$$
(18)

When M' = 0, the formulation has been derived as (17). For M' > 0, the backward components

$$MW_{A+1,A}^{M'}(M) = \left[MW_{A,A+1}^{M'-1}(M) \cdot e^{-\gamma_{A+1}l_{A+1}} \Gamma_{A+1,A+2} + MW_{A+2,A+1}^{M'}(M)\right]$$

 $\cdot e^{-\gamma_{A+1}I_{A+1}}T_{A+1,A}CM_{A+1}(M)$ (20) for $1 \le A \le$

(N-1).

Fig. 5. S-parameter network (with reference impedance Z_{ref}) cascaded to a transmission-line at Port *i*.

Then, for M'>0, the forward components $MW_{A,A+1}^{M'}\left(M\right)$

$$=\left[MW_{A+1,A}^{M^{\prime}}\left(M\right)\cdot e^{-\gamma_{A}l_{A}}\Gamma_{A,A-1}+MW_{A-1,A}^{M^{\prime}}\left(M\right)\right]$$

 $\cdot e^{-\gamma_{A}I_{A}}T_{A,A+1}CM_{A}(M)$ (21) for $1 \le A \le N$.

Therefore, the insertion loss of the cascaded system can be derived as

$$S_{21}(\omega, M, M') = \frac{1}{V_0} \sum_{k=0}^{M'} MW_{N,N+1}^k(\omega, M)$$
(22a)

Based on the definition of the S-parameters, all wave components received at the receiver needs to be considered. So, the actual transmission coefficient of the system is

$$S_{21}(\omega) = \frac{1}{V_0} \lim_{M,M' \to \infty} \sum_{k=0}^{M'} MW_{N,N+1}^k(\omega, M).$$
 (22b)

C. S-Parameter Networks in the Cascaded Channel

In many practical designs, there are some parts of the channel that are not ideal transmission-line structures, like the via transition structures. For these nonideal transmission-line structures, S-parameter networks from full-wave simulations or measurements are usually used in the channel analysis. Thus, the reflections and propagations with cascaded S-parameter network are analyzed and the formulations are extended to handle the cascaded channel with nonideal transmission-line structures.

As shown in Fig. 5, at the ports of S-parameter network, there are two kinds of reflection mechanisms: 1) the reflections due to the impedance mismatch between the external cascaded channel and the S-parameter reference impedance ($Z_C \neq Z_{ref}$); and

2) the reflections inside the S-parameter network (return loss S_{ii}).

The S-parameter reference impedance Z_{ref} is the system impedance of the network. For example, the common system impedance for a VNA is 50 Ω .

To use the similar method to analyze the wave reflections and propagations with S-parameter networks, special treatments are needed, and two different approaches are proposed.

1) Method 1: Adding Pseudosegments: By adding a pseudosegment in the middle between the external channel and the S-parameter network port, the reflections due to two different reflection mechanisms can be separated, and the previous method to derive the closed-form formulations can be applied. The length of the pseudosegment should be 0, and the characteristic impedance of the pseudosegment should be the reference impedanceoftheS-parameter. Thereflections at the S-parameter network with the additional pseudosegment are shown in Fig. 6.

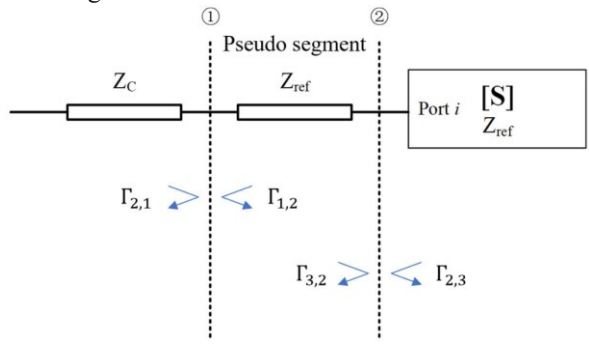


Fig. 6. Adding a pseudosegment at ports of S-parameter network to separate two kinds of reflections.

Since the length of the pseudosegment is $l_{pseudo} = 0$ and there is no loss and no phase delay for the wave propagation on the pseudosegment

$$e^{-\gamma l_{pseudo}} = 1. (23)$$

At the interface #1, there are only the reflections due to the impedance mismatch $Z_C \neq Z_{ref}$, and

$$\Gamma_{2,1} = \frac{Z_{ref} - Z_C}{Z_{ref} + Z_C} \tag{24}$$

$$\Gamma_{1,2} = \frac{Z_C - Z_{ref}}{Z_C + Z_{ref}} \tag{25}$$

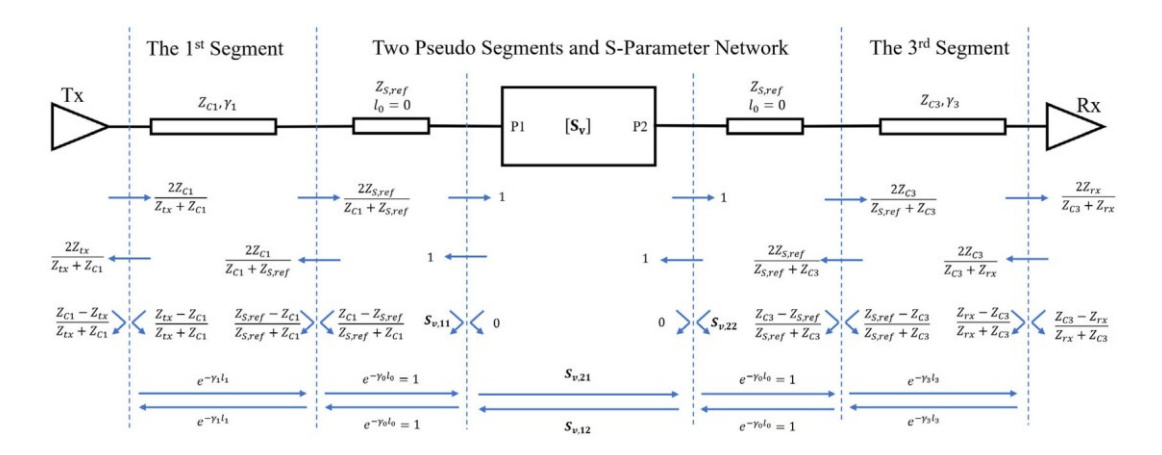


Fig. 7. Method 1: Adding pseudosegments—wave propagations and reflections in a cascaded channel with S-parameter network.

At the interface #2, there are only the reflections from inside of the S-parameter network S_{ii} , and

$$\Gamma_{3,2} = S_{ii} \tag{26}$$

$$\Gamma_{2,3} = 0. \tag{27}$$

Basedonthismethod, an example of all the wave propagations and reflections in a cascaded channel with S-parameter network is shown in Fig. 7.

After adding the pseudosegments at the ports of the cascaded S-parameter network, the same method in the previous section can be used to derive the closed-form formulation of this cascaded channel.

2) Method 2: S-Parameter Renormalization: Rather than adding additional pseudosegments at the ports of S-parameter networks, another possible approach is to remove the reflections due to the impedance mismatch by S-parameter renormalization. When $Z_C = Z_{ref}$, there will only be the reflections due to the return loss of the S-parameter network.

As mentioned in the previous section, the characteristic impedance of the external cascaded channel can be frequencydependent and complex, which is not common for S-parameter reference impedance. In addition, the characteristic impedances of the external channels can be different at different S-parameter ports. Therefore, the S-parameter renormalization needs to be doneateachsinglefrequency, and the renormalized S-parameter may have different reference impedances at different ports.

In [16], the formulation for S-parameter renormalization is introduced

$$[S_{new}] = [P]^{-1} ([S_{old}] - [\gamma]) ([I] - [\gamma][S_{old}])^{-1} [P]$$
 (28)

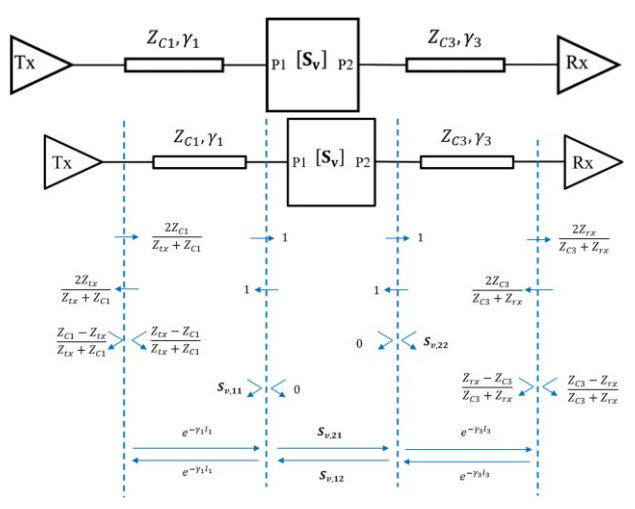


Fig. 8. Method 2: S-Parameter Renormalization—wave propagations and reflections in a cascaded channel with S-parameter network.

where $[S_{new}]$ and $[S_{old}]$ are $n \times n$ S-parameter matrices after and before the renormalization; [P] and $[\gamma]$ are diagonal matrices. Let $Z_{new,ii}$ and $Z_{old,ii}$ be the new and old reference impedances at port i

$$\gamma_{ii} = \frac{Z_{new,ii} - Z_{old,ii}}{Z_{new,ii} + Z_{old,ii}} \tag{29}$$

$$P_{ii} = \sqrt{\frac{Re\left(Z_{old,ii}\right)}{Re\left(Z_{new,ii}\right)}} \cdot \left| \frac{Z_{new,ii}}{Z_{old,ii}} \right| \cdot \frac{2Z_{old,ii}}{Z_{old,ii} + Z_{new,ii}}.$$
(30)

After the S-parameter renormalization, an example of all the wave propagations and reflections in a cascaded channel with S-parameter network is shown in Fig. 8. Also, the same method in the previous section can be used to derive the closed-form formulation of this cascaded channel. Both methods proposed above are equivalent, applicable to different scenarios as shown below.

III. VALIDATION OF THE FORMULATIONS

As shown in Fig. 9, an example of a differential channel with the S-parameter of a via transition structure from the fullwavesimulationisdesignedtovalidatethecorrectnessofthe derived formulations and the handling of cascaded Sparameter networks.

Fig. 9. Example of a differential channel with S-parameter of a via transition structure with 50 Ω reference impedance.

TABLE I PARAMETERS OF THE CHANNEL

THURSDIE OF THE OFFICE			
Parameters	Values		
Total dielectric thickness b	35.6 mils		
Trace width W	16 mils		
Trace spacing s	32 mils		
Trace thickness t	1.38 mils		
Length of trace l_1 and l_3	400 mils		
Resistance of metal ρ	$1.764 \times 10^{-8} \ \Omega m$		
$arepsilon_r'$ @ 1 GHz	3.7		
tan δ @ 1 GHz	0.02		
Djordjevic model f_L	1 kHz		
Djordjevic model f_H	1000 THz		
G_p	1.5		
ε_0	$8.854 \times 10^{-12} \text{ F/m}$		
μ_0	$4\pi \times 10^{-7} \text{ H/m}$		

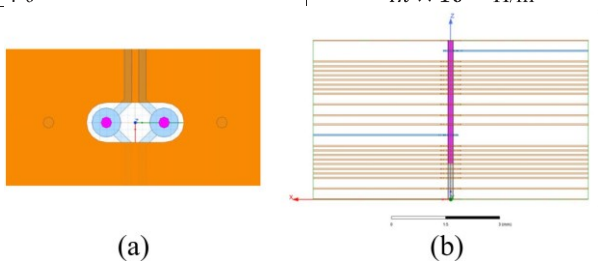


Fig. 10. Via structures in the full-wave simulation (a) top view; and (b) the side view.

The odd-mode impedances of the transmitter and the receiver are $Z_{tx} = Z_{rx} = 50 \Omega$. The first and the third segments are symmetrical differential striplines with the same cross-sectional geometries, and the related parameters can be found in Table I.

The S-parameter network is from a full-wave simulation on a via transition structure. The via structure is shown in Fig. 10.

TABLE II PARAMETERS OF THE Via

Parameters	Values
Via diameter	6 mils
Via spacing	32 mils
Anti-pad diameter	22 mils
Pad diameter	16 mils

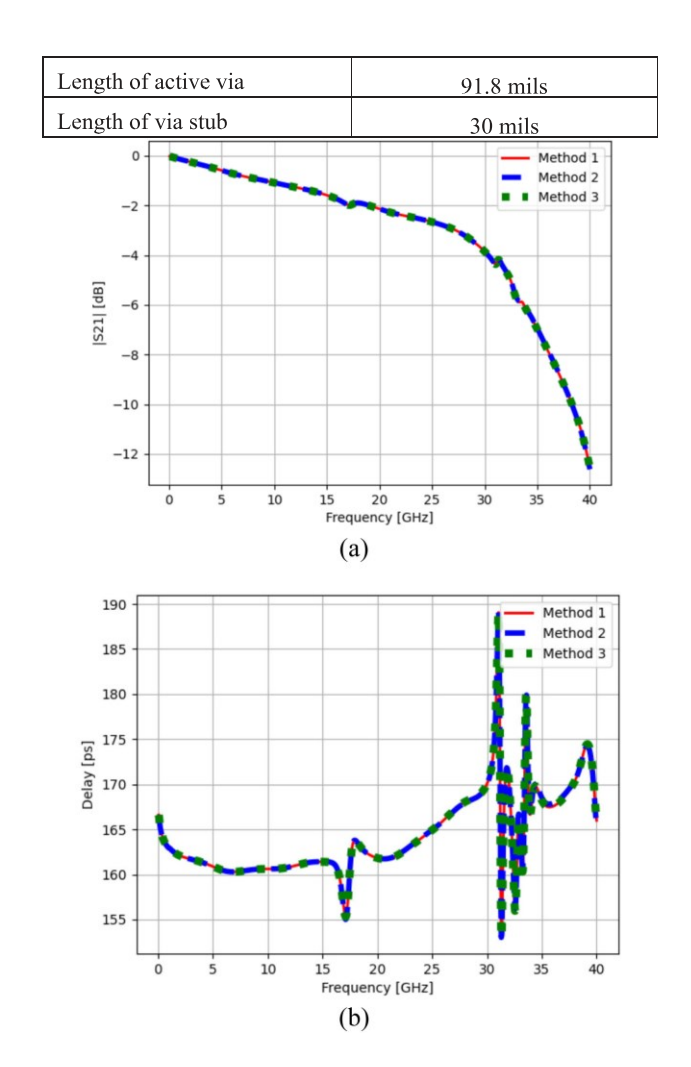


Fig. 11. Comparisons on (a) |S21| and (b) group delay from three different methods.

The geometry information of the via structure can be found in TableII. The frequency range of the full-wave simulation is from 10 MHz to 100 GHz.

Let $M \to \infty$ and M' = 20 in the calculation of S_{21} using the derived analytical formulations to ensure that enough number of wave reflections have been included in the calculation, and the results are shown in Fig. 11.

In Fig. 11, we have the following denotations on the methods:

- 1) Method 1 is the pseudosegment method. Pseudosegments are added at the ports of S-parameter networks, as shown in Fig. 7.
- 2) Method 2 is the renormalization method. S-parameters of themiddlesegmenthavebeenrenormalizedtotheexternal channel's characteristic impedances $Z_{C,1}$ and $Z_{C,3}$ at port 1 and port 2, respectively (see Fig. 8).



Fig. 12. Cascaded high-speed differential channel with three stripline segments and two via transition structures.

TARGETERS OF THE CHARMED IN FIG. 12			
Parameters	Values		
Total dielectric thickness b	23.4 mils		
Trace width W	4 mils		
Trace spacing s	4 mils		
Trace thickness t	1.38 mils		
Resistance of metal ρ	$1.764 \times 10^{-8} \ \Omega m$		
ε_r' @ 1 GHz	3.7		
tan δ @ 1 GHz	0.02		
Djordjevic model f_L	1 kHz		
Djordjevic model f_H	1000 THz		

TABLE III
PARAMETERS OF THE CHANNEL IN FIG. 12

3) Method 3 is the reference result, and it is obtained from ADS simulations.

All these results have good correlations, indicating that the proposed methods have good accuracy, and the cascaded Sparameter network is properly treated.

IV. APPLICATIONS TO CHANNEL OPTIMIZATIONS

When evaluating a high-speed signal channel, eye opening in the eye-diagram is a common criterion, and the intersymbol interference (ISI) has negative impacts on the eye opening. ISI can be identified clearly in the single-bit response (SBR) of the channel. Thus, it is possible to optimize the channel based on the SBR. The reflections in a cascaded channel generate additional ripples in the SBR after the main peak and are one of the important contributors to the ISI. Smaller ripples due to reflections in SBR means larger eye opening. Also, if DFEs are going to be added at the receiver to improve the signal quality, less voltage compensation and less power consumption will be needed.

Since the proposed method for evaluating cascaded channels is based on analyzing the wave propagations and reflections individually, the generation of each individual ripples in the SBR can be backtracked. The steps of the proposed channel optimization method are shown below. A cascaded high-speed differential channel with three stripline segments and two via transition structures is used as the example and the schematic of the cascaded channel as shown in Fig. 12.

The cross-sectional geometry of the three striplines are the same and the parameters are shown in Table III. l_1 , l_3 , and l_5 are the lengths of the three stripline segments and the values are 100 mils, 300 mils, and 600 mils, respectively. The odd-mode transmitterandreceiverimpedances $Z_{tx} = Z_{rx} = 45\Omega$, and the odd-mode characteristic impedance of the three striplines are also around 45 Ω . The steps of the optimization process are given below.

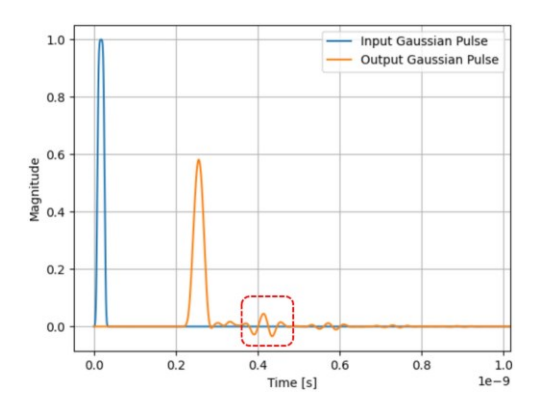


Fig. 13. Single-bit response of the cascaded channel shown in Fig. 12, and the critical ripples after the main pulse.

Step 1: Identify the critical ripples to optimize in SBR

Use the method proposed in the previous sections to calculate S_{21} of the cascaded channel. Then, the SBR of the system can be calculated, which is shown in Fig. 13. The data rate of the signal is 56 Gb/s. To avoid unwanted behavior in the SBR due to bandwidth limitation of the S-parameter, a Gaussian filter with cutoff frequency at 84 GHz (1.5 × data rate) is added on the input single-bit waveform.

Step 2: Backtrack the propagation path and reflections related to the critical ripples

In the SBR of the cascaded channel shown in Fig. 13, there is a group of ripples at around 400 ps (marked with red dashed rectangle) with relatively larger magnitudes, and these are the most critical ripples contributing to the total ISI.

As discussed in the previous sections, all the ripples in the SBR with different propagation paths and reflections can be analyzed individually. The steps to sort out all the ripples are summarized below:

- 1) Estimate the magnitudes of the transmission coefficients and reflection coefficients between all segments in the cascaded channel, and the propagation constant of each segment. These values are going to be used to estimate the magnitudes of the transmitted and reflected waves at each interface of cascading. The estimations can be done at a single chosen frequency using (7)–(10).
- 2) Fromtheincidentwavesentfromthetransmitter, calculate the estimated magnitudes of all possible transmitted waves and reflected waves at each interface between segments. This calculation on the wave magnitude estimation stops when the estimated wave magnitude becomes less than a predefined threshold value, e.g., 0.01. If the wave magnitude is less than the threshold value, it means that the wave magnitude is too small, and the wave is negligible in the total SBR waveforms. After this step, all the wave components in the cascaded channel with certain magnitudes are sorted out and their propagation paths in the cascaded channel are recorded.

3) Find the wave components at the receiver of the channel from the results of the previous step. Based on their propagation paths in the cascaded channel, the frequencydomain transfer function of each individual ripple can be calculatedusingthefrequency-dependentcoefficients, not the estimated values. Then, the time-domain waveforms of each individual ripple can be calculated using iFFT.

The first few ripples in the original SBR and their propagation paths are shown in Fig. 14, where the magnitudes of ripples are diminished away from the main pulse.

The formulation for the main pulse is

$$V_{main} = V_{in} \cdot e_{-\gamma_1 l_1} \cdot S_{v1,21} \cdot e_{-\gamma_3 l_3} \cdot S_{v2,21} \cdot e_{-\gamma_5 l_5}$$

$$T_{tx,1}T_{1,2}T_{2,3}T_{3,4}T_{4,5}T_{5,rx}$$
 (31)

It is easy to identify that the critical ripples in the SBR (see Fig. 13) is related with the propagation path #2 in Fig. 14(a), and the corresponding formulation is $V_{ripple} = V_{in} \cdot e_{-\gamma_1 l_1} \cdot S_{v1,21} \cdot e_{-\gamma_3 l_3} \cdot S_{v2,21} \cdot e_{-\gamma_5 l_5}$

•
$$T_{tx,1}T_{1,2}T_{2,3}T_{3,4}T_{4,5}T_{5,rx}$$
 • $e^{-2\gamma_3|_3}\Gamma_{2,3}\Gamma_{4,3}$.

(32)

Based on the previous assumptions, the three striplines have the same cross-sectional geometries, so $\gamma_1 = \gamma_3 = \gamma_5$. If the total length of the PCB stripline segments are kept the same, the magnitude of these ripples will be affected by the bolded term $e^{-2\gamma_3 l_3}\Gamma_{2,3}\Gamma_{4,3}$ in (32). Therefore, to mitigate the ripple magnitude, the possible approaches are: 1) increase the length of the middle segment l_3 and 2) reduce the reflections between the middle stripline and the via structures $\Gamma_{2,3}$ and $\Gamma_{4,3}$.

Step 3: Optimize the channel based on the previous analysis

1) Tuning the distance between the 2 vias (l₃): Optimizing the via structures is necessary to reduce the reflections when designing high-speed channels, but there are always some reflections after the via optimizations. Also, the most optimized via structures may not be able to be implemented in practical designs due to limitations on spacing or manufacturing.

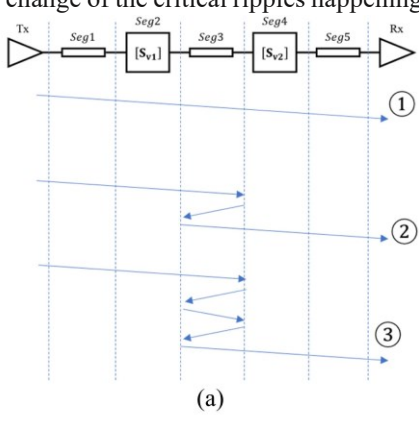
However, the analysis in the previous section indicates that it is possible to mitigate the ripple magnitudes by tuning the locationsofviasinthecascadedchannel. Whilekeepingthetotal length of the channel and the length of the first PCB stripline segment to be 1 in and 100 mils, respectively, the length of the middle stripline segment is swept from 100 mils to 800 mils, and the changes of ripples are shown in Fig. 15. The ripple energy in Fig. 15 is calculated by

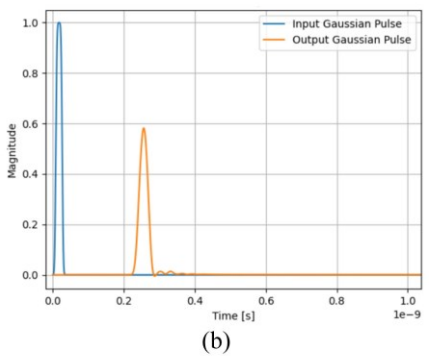
$$E_{ripple} = \int_{t_0}^{\infty} \frac{V^2 \cdot dt}{R} \tag{33}$$

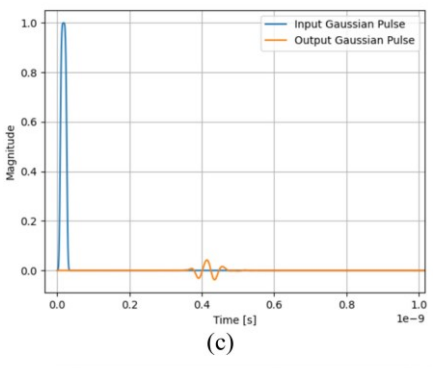
where $R = 45 \Omega$ is the system's impedance of the cascaded channel, and the unit of the calculated ripple energy from (33)

is $V^2 \cdot s/\Omega$, which is equivalent to Joule. This ripple energy is used in both Fig. 15(a) and Table IV to evaluate the ripple behaviors in the time-domain response.

In Fig. 15, the calculation of total ripple energy starts the energy integration at half UI after the peak of the main pulse, and the main pulse has not ended yet. Thus, a part of the main pulse is also included in the ripple evaluation. To completely focus on the change of the critical ripples happening around 400







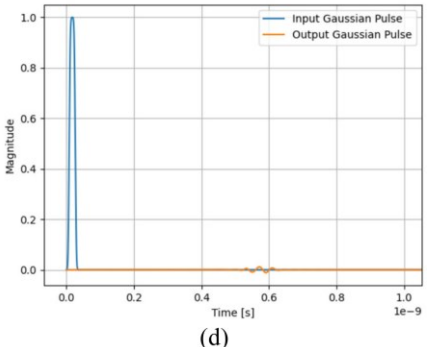


Fig. 14. (a) First three ripples propagation paths in the cascaded channel; (b) the time-domain response of the ripple with path #1; (c) the time-domain response of the ripple with path #2; (d) the time-domain response of the ripple with path #3.

ps, the ripple energy calculation starting from 301 ps is also included in Fig. 15. The main pulse has ended before 301 ps and the energy integration after that is dominant by the critical ripples.

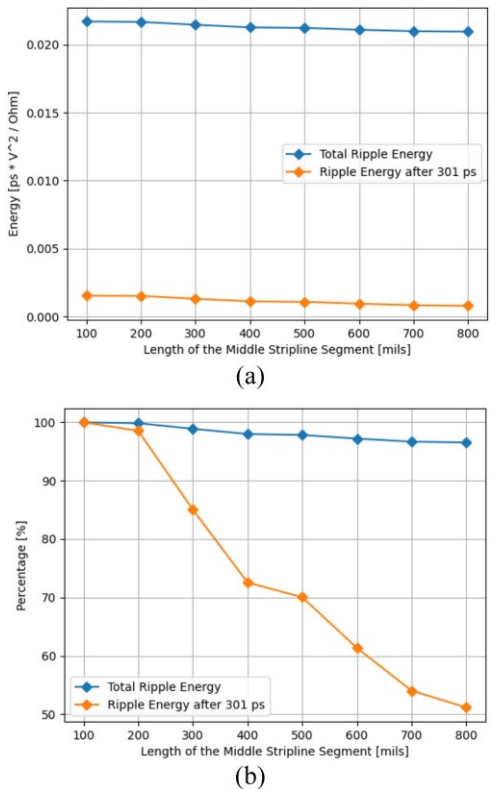


Fig. 15. Change of ripples in the SBR with different distances between the 2 vias (a) ripple energy; and (b) percentage of ripples energy reduction.

TABLE IV RIPPLES AND EYE OPENING WITH DIFFERENT W3 (TUNING $\Gamma2,3$ AND $\Gamma4,3$)

W_3	2 mils	4 mils	6 mils
Estimated $\Gamma_{2,3}$ and $\Gamma_{4,3}$	0.454	0.493	0.503
Ripple energy after the main pulse [pJ]	0.0010167	0.0011765	0.001275
Percentage of ripple energy after the main pulse	86.4%	100 %	108.4 %
Eye height [V]	0.061	0.098	0.089
Eye width [ps]	8.34	9.37	9.84
Eye area [V · ps]	0.50874	0.91826	0.87576

The change of ripples is consistent with the analysis in the previous section: when the length of the middle striplines egment increases, the magnitude and the energy of the critical ripples reduce significantly.

The eye openings of the original channel (300-mil distance between the 2 vias) and the optimized channel (800-mil

distance between the 2 vias) are also compared, as shown in Fig. 16.

The eye height and the eye width of the original channel are 0.098 V and 10.38 ps, respectively; and the eye height and the eye width of the optimized channel are 0.1255 V and 12.06 ps, respectively. Therefore, after changing the distance between the 2 vias from 300 to 800 mils, the area of the eye opening becomes 48.8% larger.

2) Tuning the reflections $\Gamma_{2,3}$ and $\Gamma_{4,3}$: The reflections $\Gamma_{2,3}$ and $\Gamma_{4,3}$ can be tuned by changing the characteristic impedance or the width of the middle segment *Seg 3* in Fig. 12. The differences comparing to the previous optimization method is

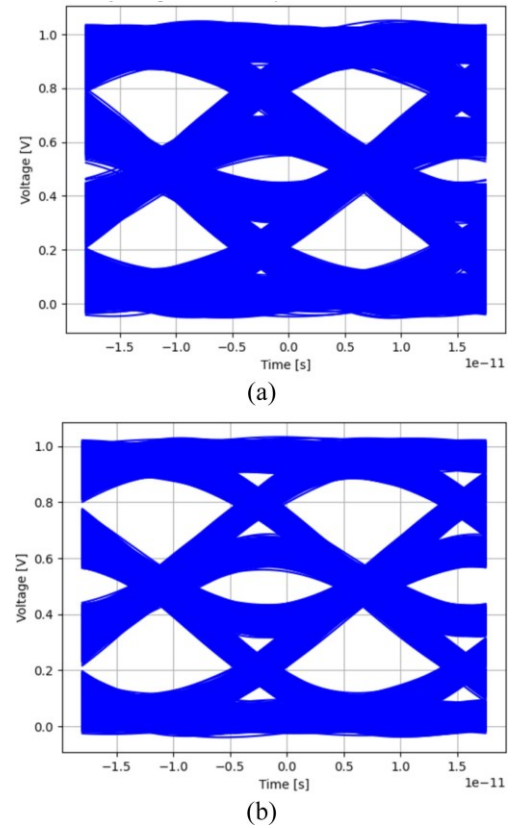


Fig. 16. Eye diagram of the 1-in channel (a) before optimization; and (b) after optimization.

that the values of other parameters ($T_{2,3}$, $T_{3,4}$, and γ_3) will change when tuning these reflection coefficients $\Gamma_{2,3}$ and $\Gamma_{4,3}$. These parameters exist in both (31) and (32), which means that thebehaviorofthemainpulsewillalsobeimpactedwhentuning $\Gamma_{2,3}$ and $\Gamma_{4,3}$.

In addition, the reflection at the S-parameter network ports couldnotbecalculated by the ratio of characteristic impedances, as revealed by (10). Since the behavior of ripples in time-domain responses is discussed and analyzed, the estimated reflection coefficient at the S-parameter port is defined as the ratio of the peak voltage level of the input pulse and the reflected waveform at the port, as shown in Fig. 17.

In the original design, the trace width of $Seg\ 3\ (W_3)$ is 4 mils, and the estimated reflection coefficient is 0.493. Two more cases with $W_3 = 2$ mils and $W_3 = 6$ mils are evaluated, and the results are summarized in Table IV.

As shown in Table IV, when the trace width of $Seg\ 3\ (W_3)$ decreases from 4 to 2 mils, the estimated reflection level at the Sparameterports decreases, and the ripple energy becomes 86.4% compared to the original design; when the trace width of $Seg\ 3\ (W_3)$ increases from 4 to 6 mils, the estimated reflection level at the S-parameter ports increases, and the ripple energy becomes 108.4% compared to the original design. The change of ripple behaviors is consistent with the expectations. However, when $W_3 = 2$ mils, the ripple is the minimum in all the three cases, but the eye opening is also the smallest. The reason is that the transmission coefficients and the propagation constant of Seg 3

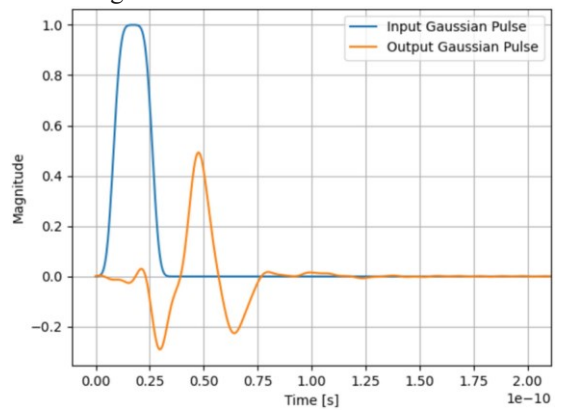


Fig. 17. Estimating the reflection coefficient at the S-parameter port based on time-domain response.

become different when tuning the trace width, and the behavior of the main pulse is also impacted. The 2-mil trace has much larger loss compared to the 4-mil trace, and the larger loss in the channel introduces a negative impact on the eye opening at the receiver side.

In this section, the channel optimizations based on the derived closed-form formulations are demonstrated using a few examples. After identifying the propagation paths and the reflections related to the critical ripples in the time-domain response by backtracking, the effective approaches to mitigate the ripples and enlarge eye openings can be determined. The effectiveness of the optimizations is validated using both single-bit response and eye diagrams. In the optimization example (see Fig. 12), tuning the distance between the 2 vias is the more effective

methodtomitigatethemagnitudesofripplesandimprovetheeye opening. The eye height or the eye opening in the eye diagram is moredirectlyrelated to the performance of a high-speed channel compared to the ripples in the channel's SBR. If the magnitude of the mainpulse in the SBR remains the same during the tuning, like tuning the distance between the 2 vias in the previous example, reducing the magnitudes of ripples in the SBR can help improve

the eye opening. If the channel tuning changes the response of the main pulse in the SBR, more attention should be paid to the tuning and the balance between larger main pulse and smaller ripples in the SBR should be determined to achieve the optimal response of the cascade channel.

V. CONCLUSION

In this article, novel formulations of multireflections in cascaded channels are proposed. The applications to optimize high-speed channels using the outlined formulations are also discussed. The formulations are derived by evaluating all wave reflections and propagations separately. Compared to the formulations published in the previous studies [13], where only the single-ended systems were investigated, we validate the correctness and accuracy of the formulation in differential cascaded systems with S-parameter networks.

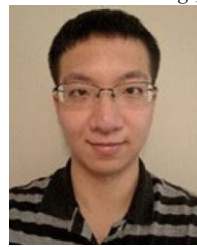
One of the most important advantages of the proposed novel formulations in this study is that ripples in the single-bit response can be backtracked according to our newly derived reflection formulations combining both frequency-domain and time-domain responses: the propagation paths and the reflections of each individual ripple in the single-bit response can be identified, and the corresponding transmission function can be determined. After identifying critical ripples in the single-bit response that need to be optimized, the channel parameters that impact the ripple behavior can be located, which would provide more precise guidance for designers to optimize the cascade dehannel.

REFERENCES

- [1] H. Wu, M. Shimanouchi, and M. PengLi, "Effective link equalizations for serial links at 112 gbps and beyond," in *Proc. IEEE 27th Conf. Elect. Perform. Electron. Packag. Syst.*, San Jose, CA, USA, 2018, pp. 25–27, doi: 10.1109/EPEPS.2018.8534219.
- [2] B. Chen et al., "Differential integrated crosstalk noise (ICN) reduction among multiple differential BGA and via pairs by using design of experiments (DoE) method," in Proc. IEEE Int. Symp. Electromagn. Compat. Signal/Power Integrity, Washington, DC, USA, 2017, pp. 112– 117, doi: 10.1109/ISEMC.2017.8077851.
- [3] B. Chen, S. Pan, J. Wang, S. Yong, M. Ouyang, and J. Fan, "Differential crosstalk mitigation in the pin field area of serdes channel with trace routing guidance," *IEEE Trans. Electromagn. Compat.*, vol. 61, no. 4, pp. 1385–1394, Aug. 2019, doi: 10.1109/TEMC.2019.2925757.
- [4] S. Yong, K. Cai, B. Sen, J. Fan, V. Khilkevich, and C. Sui, "A comprehensive and practical way to look at crosstalk for transmission lines with mismatched terminals," in *Proc. IEEE Symp. Electromagn. Compat., Signal Integrity Power Integrity*, Long Beach, CA, USA, 2018, pp. 538–543, doi: 10.1109/EMCSI.2018.8495301.
- [5] C. Johansson and T. Månefjord, "Analysis of a high-speed PCB design," in Proc. IEEE Nordic Circuits Syst. Conf. (NORCAS): NORCHIP Int. Symp. System—Chip, Linköping, Sweden, 2017, pp. 1–4, doi: 10.1109/NORCHIP.2017.8124982.
- [6] S. Yong et al., "Prepreg and core dielectric permittivity (εr) extraction for fabricated striplines' far-end crosstalk modeling," *IEEE Trans. Electromagn. Compat.*, vol. 64, no. 1, pp. 209–218, Feb. 2022, doi: 10.1109/TEMC.2021.3083771.
- [7] D.M.Pozar, Microwave Engineering, 4thed. New York, NY, USA: Wiley,

- [8] J. Ajanovic, "PCI express 3.0 overview," in *Proc. IEEE Hot Chips 21 Symp.*, Stanford, CA, USA, 2009, pp. 1–61, doi: 10.1109/HOTCHIPS.2009.7478337.
- [9] Y.-E. Yang and Q. Gu, "Time-domain perturbational analysis of nonuniformly coupled transmission lines," *IEEE Trans. Microw. Theory Techn.*, vol. 33, no. 11, pp. 1120–1130, Nov. 1985, doi: 10.1109/TMTT.1985.1133183.
- [10] R. J. Allred, B. Katz, and C. Furse, "Ripple analysis: Identify and quantify reflective interference through ISI decomposition," in *Proc. IEEE 20th Workshop Signal Power Integrity*, Turin, Italy, 2016, pp. 1–4, doi: 10.1109/SaPIW.2016.7496279.
- [11] H. Erkens and H. Heuermann, "Mixed-mode chain scattering parameters: Theory and verification," *IEEE Trans. Microw. Theory Techn.*, vol. 55, no. 8, pp. 1704–1708, Aug. 2007, doi: 10.1109/TMTT.2007.902587.
- [12] L. Yang and G. Yu, "A new method to calculate cascaded S-Parameters," in *Proc. IEEE 27th Conf. Elect. Perform. Electron. Packag. Syst.*, San Jose, CA, USA, 2018, pp. 71–73, doi: 10.1109/EPEPS.2018.8534261.
- [13] M. Ouyang et al., "An investigation on multiple reflections and group delay behavior in high-speed system designs," in Proc. IEEE Int. Joint EMC/SI/PI EMC Europe Symp., Raleigh, NC, USA, 2021, pp. 423–428, doi: 10.1109/EMC/SI/PI/EMCEurope52599.2021.9559334.
- [14] G. Yin, X. Cai, D. Secker, M. Ortiz, J. Cline, and A. Vaidyanath, "Impedance perturbation theory for coupled uniform transmission lines," *IEEETrans.Electromagn.Compat.*,vol.57,no.2,pp. 299–308,Apr.2015.
- [15] A. R. Djordjevic, R. M. Biljie, V. D. Likar-Smiljanic, and T. K. Sarkar, "Wideband frequency-domain characterization of FR-4 and time-domain causality," *IEEETrans. Electromagn. Compat.*, vol.43,no.4,pp. 662–667, Nov. 2001.
- [16] D. Woods, "Multiport-network analysis by matrix renormalization employing voltage-wave S-parameters with complex normalization," *Proc.*

Inst. Elect. Eng., vol. 124, pp. 198-204, Mar. 1977.



Muqi Ouyang (Student Member, IEEE) received the B.E. degree in electrical engineering from the Huazhong University of Science and Technology, Wuhan, China, in 2016. He is currently working toward the Ph.D. degree in the EMC Laboratory, Missouri University of Science and Technology, Rolla, MO, USA.

His research interests include signal integrity, electromagnetic interference, and computational electromagnetics.

Xiao-Ding Cai (Member, IEEE) received the Ph.D. degree in electrical engineering from the University of Ottawa, Ottawa, ON, Canada, in 1995.

He has worked with Nortel Networks, Ottawa, Sun Microsystems, Menlo Park, CA, USA, Juniper Networks, Sunnyvale, CA, USA, Rambus, Sunnyvale, and Cisco Systems, San Jose, CA, USA, as Senior Principal Engineer and Technical Leader in systems groups, specializing in high-speed signal integrity and power integrity. He has been actively promoting SI/PI methodologies, emphasizing fundamentals and applications with several technical publications and patents.



Bo Pu (Senior Member, IEEE) received the B.S. degree in electrical engineering from the Harbin Institute of Technology, China, in 2009, and the Ph.D. degree in electronic and electrical engineering from Sungkyunkwan University, South Korea, in 2015.

From 2015 to 2020, he was a Staff Engineer with Foundry Business, Semiconductor R&D headquarter of Samsung Electronics, Hwaseong, Korea. From 2020 to 2021, he was a visiting assistant research professor of National Science Foundation (NSF) In-

dustry/University Cooperative Research Center (I/UCRC) for Electromagnetic Compatibility at Missouri University of Science and Technology, MO, USA. In 2021, he joined the DeTool Technology Co. Ltd. as a vice president. His current research interest is the design methodology of the EDA for chippackage-PCB systems. He also focuses on the research works of high-speed integrated circuits system up to 224 Gbps, 2.5D Si-interposer for high bandwidth memory (HBM), and through silicon via (TSV) for 3-D ICs. He holds 10 patents about high speed links and 2.5D/3D ICs.

Dr.PuisaTPCMemberoftheJointIEEEEMCSandAPEMC2018,APEMC 2022. He was the recipient of Best Student Paper Award (2011 IEEE APEMC) and Best SIPI Symposium Paper Award (Joint 2021 IEEE EMC+SIPI and EMC Europe) as first author, a Young Scientists Award from the International Union of Radio Science (URSI) in 2014, and the 2020, 2021 Distinguish reviewer of IEEE Transactions on EMC. He also obtained Ph.D. Fellowship Award in 2013, Best Innovation Award, Excellent Performance Award, and Excellent Project Award as the first awardee in 2015–2019 from Samsung Electronics for his outstanding contributions. He was as a Session Chair in IEEE APEMC 2017,

2022, IEEEEMC+SIPI2020, 2021. He is currently an Associate Editor for IEEE ACCESS.

QianGao received the Ph.D. degree in electrical engineering from Oregon State University, Corvallis, OR, USA, in 2019.

She is currently a Hardware Engineer with Cisco System, Inc., San Jose, CA, USA.Herresearchinterestsincludesignal and power integrity, silicon photonics, and optical transceivers.

Srinath Penugonda received the Ph.D. degree from the EMC Laboratory, Missouri University of Science and Technology, Rolla, MO, USA, in 2021. His research interests include signal integrity, power integrity automotive EMC, electromagnetics and signal integrity, and high speed PCB design.

Dr. Penugonda was the winner of "Best Student Hardware Design Competition" organized by IEEE EMC Society in the year 2015. Currently, he is working in Cisco Systems Inc., as a hardware engineer.



Chaofeng Li (Student Member, IEEE) received the B.S. degree in electronic science and technology from the Guilin University of Electronic Technology, Guilin, China, in 2016, and the M.S. degree in electromagnetic field and microwave technology from the University of Electronic Science and Technology of China, Chengdu, China, in 2019. He is currently working toward the Ph.D. degree in electrical engineering from the Missouri University of Science and Technology (formerly University of

Missouri Rolla), Rolla, MO, USA.

His current research interests include signal Integrity, high-speed channel modeling, PCB material characterization, and chip-PDN impedance modeling.

Bidyut Sen received the Ph.D. degree in physics from the State University of New York, Stony Brook, NY, USA, in 1986.

He is a Principal Engineer with the Unified Compute Server Group, Cisco Systems, Inc., San Jose, CA, USA. He has many years of experience in the computer industry and has worked in several companies, including Sun Microsystems, Sunnyvale, CA, USA, Fujitsu, San Jose, and LSI Logic, San Jose.

He has several publications, presentations, and patents.



Chulsoon Hwang (Senior Member, IEEE) received the B.S., M.S., and Ph.D. degrees in electrical engineering from the Korea Advanced Institute of Science and Technology, Daejeon, South Korea, in 2007, 2009, and 2012, respectively.

He was with the Global Technology Center, Samsung Electronics, Suwon, South Korea, from 2012 to 2015, as a Senior Engineer, where he was mainly engaged in radio frequency interference (RFI) design for mobile phones. In July 2015, he joined the

MissouriUniversityofScienceandTechnology(formerly University of MissouriRolla), Rolla, MO, USA, and is currently an Assistant ProfessorwiththeMissouriS&TEMCLaboratory.Hisresearchinterestsinclude RF desense, signal/power integrity in high-speed digital systems, EMI/EMC, hardware security, and machine learning.

Dr.HwangwasarecipientoftheAP-EMCYoungScientistAward,theGoogle Faculty Research Award, and Missouri S&T's Faculty Research Award. He was a co-recipient of the IEEE EMC Best Paper Award, the AP-EMC Best Paper Award, and a two-time co-recipient of the DesignCon Best Paper Award.



Dong Hyun Kim (Member, IEEE) received the B.S., M.S., and Ph.D. degrees in electrical engineering from the Korea Advanced Institute of Science and Technology (KAIST), Daejeon, South Korea, in 2012, 2014, and 2018, respectively. In 2018, he joined the Missouri University of Science and Technology (formerly University of Missouri-Rolla), Rolla, MO, USA, and is currently an Assistant Professor with the Missouri S&T EMC Laboratory, Rolla, MO, USA.

His current research interests include nanometer-

scale devices, through-silicon via (TSV) technology, dielectric material characterization and signal integrity (SI), power integrity (PI), temperature integrity (TI), electromagnetic compatibility (EMC), and electrostatic discharge (ESD) in 2.5D/3D IC systems.

Dr. Kim is a recipient of the IEEE Region 5 Outstanding Young Professional (formerly GOLD) Award, IEEE St. Louis Section Outstanding Young Engineer Award, DesignCon Best Paper Award. He is a co-recipient of the DesignCon Early Career Best Paper Award and IEEE EMC Symposium Best SIPI Student Paper Awards. He is currently the Vice Chair or IEEE St. Louis Section, and the secretary of the IEEE EMC Society TC-10 (Signal Integrity and Power Integrity).